

# Evidence for Melt Leakage from the Hawaiian Plume above the Mantle Transition Zone

Saswata Hier-Majumder<sup>a,b</sup>, Maxim D. Ballmer<sup>c,d</sup>, Matthew Agius<sup>e</sup>,  
Catherine Rychert<sup>e</sup>, Nicholas Harmon<sup>e</sup>

<sup>a</sup>*Department of Earth Sciences, Royal Holloway University of London, Egham, Surrey,  
TW20 0EX, UK.*

<sup>b</sup>*AAAS Science and Technology Policy Fellow, Advanced Scientific Computing and  
Research, Office of Science, Department of Energy, Germantown, MD, USA.*

<sup>c</sup>*ETH Zürich, Switzerland*

<sup>d</sup>*University College London, UK*

<sup>e</sup>*University of Southampton, UK*

---

## Abstract

Dehydration reactions at the top of the mantle transition zone (MTZ) can stabilize partial melt in a seismic low-velocity layer (LVL), but the seismic effects of temperature, melt and volatile content are difficult to distinguish. We invert P-to-S receiver function phases converted at the top and bottom of a LVL above the MTZ beneath Hawaii. To separate the thermal and melting related seismic anomalies, we carry out over 10 million rock physics inversions. These inversions account for variations arising from the Clapeyron slope of phase transition, bulk solid composition, dihedral angle, and mantle potential temperature. We use two independent seismic constraints to evaluate the temperature and shear wave speed within the LVL. The thermal anomalies reveal the presence of a hot and seismically slow plume stem surrounded by a “halo” of cold and fast mantle material. In contrast to

---

*Email address: Saswata.Hier-Majumder@rhul.ac.uk (Saswata Hier-Majumder)*

this temperature distribution, the plume stem contains less than 0.5 vol% melt, while the surrounding LVL—within the coverage area—contains up to 1.7 vol% melt, indicating possible lateral transport of the melt. When compared to the melting temperatures of mantle rocks, the temperature within the LVL, calculated from seismic observations of MTZ thickness, suggests that the observed small degrees of melting are sustained by the presence of volatiles such as CO<sub>2</sub> and H<sub>2</sub>O. We estimate the Hawaiian plume loses up to 1.9 Mt/yr H<sub>2</sub>O and 10.7 Mt/yr CO<sub>2</sub> to the LVL, providing a crucial missing flux for global volatile cycles.

*Keywords:* Mantle Plume, Transition Zone, LVL, Volatiles, Melting

---

## 1. Introduction

Mantle plumes are major pathways for heat (Ballmer et al., 2013) and volatile (Burton et al., 2013; Dasgupta and Hirschmann, 2010; Kelemen and Manning, 2015; Plank and Manning, 2019) transfer from the lower mantle to the surface of the Earth. The interaction between ascending plumes and the surrounding mantle can have significant implications for global volatile cycles. Drastic reduction in the water storage capacity between minerals within and above the mantle transition zone (MTZ) (Kohlstedt et al., 1996) can lead to dehydration melting within the ascending plume (Bercovici and Karato, 2003; Ohtani et al., 2004). Sharp reduction in the melting temperature of carbonated basalts just above the MTZ (Thomson et al., 2016) can also trigger decarbonation melting of recycled oceanic crust components in the plume material atop the MTZ. A partially molten region above the MTZ may provide a reservoir for incompatible elements and volatiles, as they preferentially

15 partition into melts (Aubaud, 2004; Hirschmann and Dasgupta, 2009). The  
16 seismically anomalous low velocity layer (LVL)—characterized by 2–3% re-  
17 duction in shear wave speed (Agius et al., 2017; Hier-Majumder and Courtier,  
18 2011; Hier-Majumder et al., 2014; Tauzin et al., 2010; Vinnik and Farra, 2007)  
19 and small amounts ( $\sim 1$  vol%) of partial melt (Hier-Majumder and Courtier,  
20 2011; Hier-Majumder et al., 2014)—is one such possible reservoir. Among  
21 the several tectonic settings in which LVLs are observed (Tauzin et al., 2010;  
22 Vinnik and Farra, 2007), their potential role in storing mantle volatiles near  
23 subduction zones has been discussed (Hier-majumder and Tauzin, 2017; Sun  
24 et al., 2020), but volatile fluxes to the LVLs associated with plumes remains  
25 relatively poorly quantified (Dasgupta and Hirschmann, 2010).

26 Sequestration of partial melt from the plume into the LVL can impede  
27 the volatile transport to the Hawaiian volcanoes from the lower mantle. The  
28 high volatile content of the Hawaiian plume, evidenced by 2.4 Mt/yr CO<sub>2</sub>  
29 emissions from Kilauea volcano (Burton et al., 2013), is derived from re-  
30 cycled oceanic crust (Sobolev et al., 2007), which contains up to 450 ppm  
31 H<sub>2</sub>O (Bizimis and Peslier, 2015) and 250 ppm CO<sub>2</sub> (Anderson and Poland,  
32 2017). Volatile-rich melt generation in the LVL and subsequent interaction  
33 between these melts and the plume is indicated by geochemical signatures  
34 with mixing trends between multiple reservoirs (Hauri, 2002). Despite this  
35 geochemical evidence, geophysical observations of melt loss from the plume  
36 and quantification of associated volatile fluxes remained elusive.

37 While heat and mass transfer by mantle plumes to the upper mantle is  
38 thought to be interrupted by volatile-rich melt pooling above the mantle tran-  
39 sition zone (MTZ) (Bercovici and Karato, 2003), quantifying the magnitudes

40 of melt and dissolved volatile fluxes from seismic anomalies remain challeng-  
41 ing, as both elevated temperature and melt have similar seismic signatures  
42 (Tauzin et al., 2010; Vinnik and Farra, 2007; Wei and Shearer, 2017; Wolfe  
43 et al., 2009, 2011). Previous seismic and rock physics studies of plume-related  
44 LVLs either focused on mapping anomalous seismic wave speeds in the LVL  
45 (Laske et al., 2009; Tauzin et al., 2010; Vinnik and Farra, 2007) or calculating  
46 an average melt fraction (Hier-Majumder et al., 2014). Distinction between  
47 the spatial variations due to temperature and melt content has remained  
48 difficult, as both sustain low seismic wave speeds. In this work, we over-  
49 come this limitation by carrying out a detailed analysis of teleseismic P-to-S  
50 phase conversions obtained from permanent and temporary land and ocean  
51 bottom broadband seismometers from the “Plume-lithosphere undersea melt  
52 experiment” (PLUME) (Agius et al., 2017; Laske et al., 2009), quantifying  
53 the distribution of both temperature and melt in the LVL beneath Hawaii.  
54 Both the high lateral resolution of the previous receiver function work (Agius  
55 et al., 2017) combined with our formal accounting of error in the inversions  
56 allow us to map the distribution of both temperature and melt in the LVL  
57 beneath Hawaii with unprecedented resolution. While a previous study by  
58 Hier-Majumder et al. (2014) estimated  $\sim 1$  vol% melting in the Hawaiian  
59 LVL, the limited lateral resolution of seismic data in this work was insuffi-  
60 cient to map the lateral distribution of melt.

61 In the following section, we present a detailed discussion of the methods  
62 of seismic and rock physics analysis, a description of the parameter space,  
63 and the method of uncertainty calculation arising from uncertainties in the  
64 rock physics inversion. Section 3 outlines the results of the rock physics

65 inversion, including a detailed description of the effect of each parameter  
66 on the calculated melt volume fraction. Based on our results, we present  
67 a hypothesis on plume leakage and its impact on the global volatile cycles  
68 in Section 4. Finally, we outline the key findings of this work in Section 5.  
69 We also derive a zeroth-order equation for volatile flux associated with melt  
70 leakage in Appendix A.

## 71 **2. Methods**

### 72 *2.1. Receiver functions*

73 The dataset exploited here is acquired from the previous study of Agius  
74 et al. (2017). For this dataset, teleseismic P-to-S phase conversions were  
75 obtained from permanent and temporary land and ocean bottom broad-  
76 band seismometers located across the Hawaiian archipelago (*e.g.* Hawai-  
77 ian Plume-Lithosphere Undersea Mantle Experiment–PLUME (Laske et al.,  
78 2009, 2011)). The seismic model extends outside the region shown, for in-  
79 stance  $>24$  degrees North (Agius et al., 2017). We only present the robust  
80 regions for the purposes of this work, thus avoiding artefacts owing to ar-  
81 eas of lower resolution. Preprocessing of the waveforms for ocean stations  
82 included removal of the tilt noise on the vertical components (Crawford and  
83 Webb, 2000), removal of the compliance noise (Bell et al., 2015), and reorien-  
84 tation of the horizontal components. Both land and ocean stations were then  
85 band-pass filtered between 0.05–0.2 Hz and had the horizontal components  
86 rotated to the radial and transverse components. Waveforms of teleseismic  
87 earthquakes with a magnitude greater than  $M_w = 5.5$  and with an epicentral  
88 distance to the stations between  $35^\circ$  and  $80^\circ$  were extracted for further analy-

89 sis. Manually selected P phases were deconvolved from the radial component  
90 using the extended multitaper frequency domain deconvolution technique  
91 (Rychert et al., 2013) to produce a receiver function. A positive amplitude  
92 receiver function phase indicates a wave speed increase with depth, whereas  
93 a negative amplitude indicates a wave speed decrease.

94 Each receiver function was migrated to depth, and corrected for the  
95 sphericity of the Earth, thus diminishing edge effects. A one-dimensional,  
96 crust-corrected reference model (PREM, (Dziewonski and Anderson, 1981;  
97 Leahy et al., 2010), Crust 1.0 (Laske et al., 2013)) was applied with addi-  
98 tional corrections for the stations' elevations (Figure 1). As an example of  
99 absence of edge effects, Figure 1 shows the 410 km discontinuity 'rises' and  
100 'deepens' again towards the edge. Estimates for the uncertainties of the re-  
101 ceiver functions were determined with bootstrap resampling and averaging  
102 of the receiver function traces within a bin. The migrated receiver functions  
103 were then back-projected along the theoretical ray path and stacked onto a  
104 three-dimensional (3-D) grid with a lateral spacing of  $1^\circ$  by  $1^\circ$  and a 1 km  
105 depth vertical spacing. The grid is smoothed with a radius corresponding  
106 to the Fresnel zone of the waveform (Figure 1). The depth and amplitude  
107 of the positive peak close to the 410 and 660 km depth were selected as the  
108 mantle transition zone discontinuities. Similarly, the depth and amplitude  
109 of the negative peak atop the 410 were selected specifically for this study.  
110 Sporadic positive polarity phases in the 200-350 km depth range in the model  
111 of Agius et al. (2017), are likely related to small scale heterogeneity, as has  
112 frequently been observed and described by other Rev1 (*e.g.* Deuss, 2009). We  
113 also observe phases within the transition zone similar to detections reported

114 by previous studies (Shearer, 1990). The standard error of the amplitudes  
115 and of the discontinuity depths are shown in the supplementary material.

116 Based on this analysis of the dataset, we attempt to determine lateral  
117 variations in the presence or absence of melt across the region. Such deter-  
118 mination becomes achievable with our 3-D receiver function migration ap-  
119 proach using a wide aperture array (Agius et al., 2017). Also note that our  
120 inversion scheme fully accounts for and propagates errors quantitatively. Al-  
121 though near-plume melt imaging is seemingly inconsistent with one previous  
122 receiver function study that found no evidence for a melt layer above the 410  
123 near plumes, the scale of our observation would not likely be resolvable by  
124 the single station stack approach of the previous study (Tauzin et al., 2010).  
125 We previously verified the robustness of interpreted transition-zone thick-  
126 ness variations by implementing a variety of migrations models (Agius et al.,  
127 2017). These models involve 1-D (PREM), 3-D with a central low shear wave  
128 speed plume, and 3-D with a plume surrounded by fast shear wave speeds, af-  
129 ter anomaly magnitudes reported by Wolfe et al. (2009). These tests showed  
130 that the observed variability in transition zone thickness are robust.

## 131 *2.2. Rock physics analysis*

132 We carried out rock physics analysis using the numerical code MuMaP  
133 (version 2.1, Hier-Majumder, 2020; Hier-Majumder et al., 2014). In this  
134 method, we use two independent sets of seismic observations to constrain  
135 the temperature and shear wave speed at each location. We then use the  
136 mineral physics model of Xu et al. (2008) in combination with the calculated  
137 temperature to isolate the effect of the bulk composition and temperature on  
138 the seismic signature. Any residual negative anomalies are then attributed to

139 melting. In the following subsections, we describe these details in sequence.  
140 Interested readers can see Hier-Majumder et al. (2014) for a more detailed  
141 description of the analysis. Interested readers can access the raw data from  
142 rock physics inversions from an open-source database (Hier-Majumder et al.,  
143 2019).

#### 144 *2.2.1. Temperature*

145 The first step in our analysis involves calculating the temperature at  
146 each of the 1681 locations of the dataset. We used two different methods  
147 to estimate this temperature at each location (*i.e.*, in two separate sets of  
148 rock physics inversions): (1) the thickness of the MTZ (Hier-majumder and  
149 Tauzin, 2017; Tauzin and Ricard, 2014) and (2) the topography of the 410  
150 km discontinuity (Hier-Majumder et al., 2014). On one hand, using the MTZ  
151 thickness minimizes errors from unknown wave speed anomalies above 410  
152 km depth, including in the crust, which may influence the seismically-inferred  
153 depth of the 410 km (Tauzin and Ricard, 2014). On the other hand, using  
154 the MTZ thickness as a proxy for temperature neglects any potential radial  
155 temperature gradients across the MTZ.

156 To quantify the uncertainties arising from temperature, we computed  
157 the temperature for 9 different Clapeyron slopes of the olivine-wadsleyite  
158 transition in the range of 0.5 to 4.5 MPa/K for both sets of measurements.  
159 Once the temperature anomalies are calculated, we convert these anomalies  
160 to temperature by adding an adiabat with a specified potential temperature  
161 and an adiabatic gradient of 0.3 K/km. To test the effects of potential  
162 temperature, we carry out inversions for 5 different values of the potential  
163 temperature ranging from 1127 to 1527 °C (1400–1800 K).



164 *2.2.2. Bulk solid composition*

165 In addition to temperature, we explore the effects of the excess fraction  
166 of eclogite in the LVL mantle,  $f$ , on the resultant seismic wave speeds. In  
167 our compositional model, the fraction  $f$  of the mantle consists of purely  
168 basaltic component, while the rest,  $1 - f$ , consists of peridotite. We use the  
169 compositional model from Xu et al. (2008), which suggests that the peridotite  
170 consists of a mechanical mixture of 18% basalt and 82% harzburgite. The  
171 bulk basalt fraction  $X$ , the quantity commonly used in the geophysics and  
172 mineral-physics literature, and the excess eclogite fraction  $f$ , are then related  
173 by

$$0.18(1 - f) + f = X, \quad (1)$$

174 where  $X$  is expressed as a fraction. In the inversions, we use  $X$  to evaluate  
175 physical properties according to Xu et al. (2008). In the figures, we use  $f$  to  
176 indicate the excess fraction of mantle eclogite. According to Sobolev et al.  
177 (2007), the plume source material contains approximately 20% eclogite. In  
178 the deep eclogitic pool (DEP) atop the transition zone (Ballmer et al., 2013),  
179 discussed in Section 4, the solid matrix should be more enriched in eclogite  
180 than the plume stem and is expected to have a higher value of  $f$  than 0.2.  
181 We report the results for a conservative estimate of  $f = 0.27$  ( $X = 0.4$ ) for  
182 the composition of the LVL matrix. As discussed in Section 3.2 in the region  
183 around the plume stem, a higher value of  $f$  will lead to a higher predicted  
184 median melt volume fraction than our conservative estimate. As a result,  
185 our calculated LVL melt fractions remain a conservative estimate.

186 Once the temperature is evaluated at each point and a bulk solid com-  
187 position is assigned to the mantle, we proceed to calculate the melt volume

188 fraction from the residual seismic anomaly, described next.

### 189 *2.2.3. Melting*

190 To calculate melt volume fractions, we start by defining a reference shear  
191 wave speed,  $V_S^{ref}(X, T)$  and an inferred shear wave speed,  $V_S^{inf}$ . The reference  
192 shear wave speed is a theoretical value, dependent on the temperature ( $T$ )  
193 and solid composition ( $X$ ). Since we calculate the temperature at each point  
194 from either the MTZ thickness or the MTZ topography, this value is spatially  
195 variable. In contrast, we calculate the inferred shear wave speed from the  
196 normalized amplitude,  $R_{norm}$ , of the receiver function (Hier-Majumder et al.,  
197 2014). As the value of the normalized amplitude is spatially variable, so  
198 is  $V_S^{inf}$ . Notice, however, this spatial variation is independent of and, as  
199 shown later, generally different from the spatial variations in  $V_S^{ref}(X, T)$ .  
200 If, at a location,  $V_S^{ref}(X, T) = V_S^{inf}$ , no melting is necessary to explain  
201 the seismic observation. If, however, these two wave speeds are unequal  
202 and  $V_S^{ref}(X, T) > V_S^{inf}$ , we attribute the anomaly to melting. To quantify  
203 the amount of melting from the difference between these two independently  
204 derived wave speeds, we define a melt anomaly function,  $\xi(\theta, \phi)$ , such that

$$V_S^{inf} - \xi(\theta, \phi)V_S^{ref}(X, T) = \epsilon, \quad (2)$$

205 where  $\epsilon \ll 1$  is the residual error of the calculation,  $\theta$  is the solid-melt dihedral  
206 angle, and  $\phi$  is the unknown melt-volume fraction. Using this definition, we  
207 can define the residual shear wave speed anomaly as (setting  $\epsilon = 0$ )

$$\Delta V_S = \frac{V_S^{inf} - V_S^{ref}}{V_S^{ref}} = \xi(\theta, \phi) - 1. \quad (3)$$

208 Having incorporated the effects of temperature and bulk solid composition in  
209 computing  $V_S^{ref}$ ,  $\Delta V_S$  is independent from variations in temperature and solid

210 composition within the parameter space of our inversion. Next, assigning a  
211 range of known values to the parameters  $X$ ,  $T$  and  $\theta$ , we invert the nonlinear,  
212 implicit equation (2) to calculate the unknown melt-volume fraction,  $\phi$ , at  
213 each location.

#### 214 *2.2.4. Parameter space*

215 To explore the parameter space, we carried out the inversions for 5 dif-  
216 ferent values of mantle potential temperature, 7 dihedral angles between  $10^\circ$   
217 and  $40^\circ$ , 10 different values of  $X$  ranging from 0.1 to 0.99, and 9 different val-  
218 ues of Clapeyron slope. All these analyses were carried out using 2 different  
219 methods to evaluate lateral thermal anomalies in the transition zone (based  
220 on either the MTZ thickness, or the topography of the 410-km discontinuity,  
221 see above), totaling 6300 analyses for each of the 1681 data locations (or more  
222 than 10 million inversions). Using this large parameter space not only allows  
223 us to quantify the variations in calculated melt fractions, but also provides a  
224 robust estimate of the uncertainties arising from these variations, discussed  
225 in section 2.3.

#### 226 *2.2.5. Calculation of permeability and melt segregation velocity*

227 Once the melt fraction is evaluated at each point, we use the calculated  
228 melt volume fraction to obtain the permeability and a zeroth order estimate  
229 of melt migration velocity for the given melt fraction. We calculated the  
230 permeability of melt from the melt fraction using a microstructural model of  
231 melt in tubes at three-grain corners (Turcotte and Schubert, 2001, eq. 9-10).  
232 In this model, the permeability,  $k$ , is related to the melt fraction,  $\phi$ , by the  
233 relation,  $k = (b^2\phi^2) / 72\pi$ , where we assume  $b = 1$  mm is the matrix grain

234 size (Hier-majumder and Tauzin, 2017). To evaluate the melt migration  
235 velocity, we use a 1D model of two-phase flow and compaction (Bercovici  
236 et al., 2001; Hier-Majumder et al., 2006). In this model, each point is treated  
237 as a melting column where the melt segregation from the matrix is governed  
238 by compaction within the matrix and density-driven segregation between the  
239 melt and the matrix. Following the method outlined by Hier-Majumder and  
240 Courtier (2011), we solve the governing partial differential analytically to  
241 obtain an expression for the melt segregation velocity as a function of melt  
242 volume fraction within the column. For the melt fraction at each location,  
243 we use the result of the rock physics inversion. The interested reader is  
244 encouraged to see the details of this solution in the work of Hier-Majumder  
245 and Courtier (2011).

### 246 *2.3. Calculation of uncertainties*

247 One of the strengths of our analysis is the identification of the first-order  
248 uncertainties and quantification of the error in the calculated melt volume  
249 fraction. We do not consider the putative influence of crystal-bound water  
250 or melt composition in the reduction of seismic wave speeds. Recent exper-  
251 imental results at LVL-like pressure temperature conditions show that the  
252 influence of water on seismic wave speed reduction is small (Schulze et al.,  
253 2018). In addition, there is a lack of documented systematic variation of  
254 the wave speed in solids as a function of water related point defects in the  
255 nominally anhydrous minerals under LVL-like conditions, precluding a pa-  
256 rameter space search for uncertainty as carried out in this work. In two pre-  
257 vious studies, Hier-Majumder et al. (2014) and Wimert and Hier-Majumder  
258 (2012) experimented with the influence of melt composition on the calcu-

259 lations using equations of states of different melts. For small melt volume  
 260 fractions such as the LVL, the influence of melt composition was found to  
 261 be insignificantly small. In other words, we only focus on the factors that  
 262 exert a first-order influence on the calculated wave speed and are sufficiently  
 263 characterized, thus permitting a systematic parameter-space search.

264 We calculated the uncertainty in the melt volume fractions,  $\alpha_\phi$ , from the  
 265 uncertainties ( $\alpha_i$ ) in the four parameters ( $\eta_i$ ): potential temperature ( $\eta_T$ ),  
 266 basalt fraction ( $\eta_X$ ), dihedral angle ( $\eta_\theta$ ), and the Clapeyron slope of olivine-  
 267 wadsleyite transformation ( $\eta_\gamma$ ). The propagated error is calculated from the  
 268 uncertainties and gradients  $\partial \langle \phi \rangle / \partial \eta_i$ , using the formula

$$\alpha_\phi = \sqrt{\sum_i \alpha_i^2 \left( \frac{\partial \langle \phi \rangle}{\partial \eta_i} \right)_{j \neq i}^2} \quad (4)$$

269 where  $\partial \langle \phi \rangle / \partial \eta_i$  is the rate of change of the median melt volume fraction with  
 270 changes in one of these four parameters, keeping the other three constant. We  
 271 use uncertainty values of  $\alpha_\theta = \pm 5^\circ$  (Minarik and Watson, 1995),  $\alpha_\gamma = \pm 0.8$   
 272 MPa/K (Tauzin and Ricard, 2014), and  $\alpha_X = \pm 16\%$  (Sobolev et al., 2007)  
 273 and calculate the derivatives  $\partial \langle \phi \rangle / \partial \eta_i$  numerically from our inversions. We  
 274 evaluate the uncertainty in temperature,  $\alpha_T$ , from the standard deviation in  
 275 the measurement of the MTZ thickness,  $h_{MTZ}$ . For a mantle density of  $\rho$ ,  
 276 gravity,  $g$ , and a Clapeyron slope of  $\gamma$ , we estimate

$$\alpha_T = h_{MTZ} \frac{\rho g}{\gamma}. \quad (5)$$

277 Using  $\rho = 3300 \text{ kg/m}^3$ ,  $g = 10 \text{ ms}^{-2}$ ,  $\gamma = 3 \text{ MPa/K}$ , and  $h_{MTZ} = 5.8 \text{ km}$   
 278 from our data, we get  $\alpha_T = 63.8^\circ\text{C}$ , which we use in equation (4). Inserting  
 279 these values in equation (4), we evaluate the error in melt volume fraction  
 280  $\alpha_\phi = \pm 0.3 \text{ vol}\%$ .

281 **3. Results**

282 We carried out two sets of analyses—using two different methods for  
283 determining temperature as described in Section 2.2.1—and found that dif-  
284 ferences between the results are small. For example, the inferred median  
285 melt-volume fractions calculated from these two methods differ only by  $\sim 0.01$   
286 vol%, an order of magnitude smaller than the propagated error. In this sec-  
287 tion, we report temperatures calculated using our preferred method, MTZ  
288 topography, unless stated otherwise.

289 *3.1. Melt distribution within the Hawaiian LVL*

290 The primary seismic observations and a few calculated quantities are  
291 mapped in Figure 2. The MTZ beneath Hawaii (Figure 2(a), median thick-  
292 ness 251 km) is characterized by a thin central region surrounded by a thicker,  
293 concentric region. While such a feature is absent in the map of LVL thickness  
294 in Figure 2(b), the thickest part of the LVL trends SE-NW, being elongated  
295 roughly in the direction of plate motion. This correlation between LVL thick-  
296 ness and plate motion suggests that the LVL is possibly a dynamic feature  
297 interacting with the ambient mantle flow. We find that the temperature dis-  
298 tribution near the 410 km discontinuity displays a bimodal spatial pattern.  
299 Consistent with previous seismic P and S-wave tomography models (Wolfe  
300 et al., 2009, 2011); the hot and seismically slow plume stem is surrounded by  
301 a “halo” of cold and fast material (Figure 2(c)) (Agius et al., 2017).

302 The separation between the thermal and chemical component of the  
303 Hawaiian LVL becomes clear from the map of the inferred and reference  
304 seismic wave speeds. As expected, the map of reference wave speed,  $V_S^{ref}$ ,

305 (Figure 2(d)) closely follows the temperature distribution, with slow wave  
 306 speeds within the plume stem and fast wave speeds in the cold halo. Such a  
 307 halo is often interpreted as a curtain of cold downwelling from the base of the  
 308 lithosphere to the MTZ (Ballmer et al., 2013). In contrast to the tempera-  
 309 ture, the normalized amplitude of Ps conversions (Figure 2(e), median  $-0.88$   
 310 (Agius et al., 2017)) displays a more diffuse spatial pattern. Indeed, the halo  
 311 is much less distinctive in the map of the inferred shear wave speed,  $V_S^{inf}$   
 312 (Figure 2(f)). If variations in seismic properties were purely due to thermal  
 313 effects,  $V_S^{ref}$  and  $V_S^{inf}$  should be the same within the limit of uncertainties.  
 314 The difference between these two wave speed distributions, observed at this  
 315 resolution for the first time, highlights the separation between the thermal  
 316 and melting anomalies.

317 Our analysis shows that the patches which contain the highest melt frac-  
 318 tions lie outside the hot plume stem. The residual anomaly,  $\Delta V_S$ , (Figure  
 319 3(a)) is mostly negative (median value of  $-1.8 \pm 0.9\%$ ) within the LVL, imply-  
 320 ing the presence of partial melt. The melt distribution (median value of  $0.4$   
 321  $\pm 0.3\%$ ) closely follows the distribution of  $\Delta V_S$ , as illustrated in Figure 3(b).  
 322 Parts of the LVL containing melt-volume fractions that exceed 1 vol% are  
 323 associated with the region between the plume stem and the halo (indicated  
 324 by isotherms in Figure 3(b)). In turn, the melt volume fraction is  $\leq 0.5$  vol%  
 325 within the plume stem (and even lower within the cold halo). This observa-  
 326 tion contradicts the expected spatial association between regions of high melt  
 327 volume fraction with regions of high temperatures, suggesting instead, that  
 328 the melt must have been carried away from the plume stem. Notice that this  
 329 lateral extent of partial melt, and thus, the potential extent of passive lateral

330 melt transport is limited to the region covered by the data. The fact that  
331 this melt displacement must be associated with mantle flow, is demonstrated  
332 by a calculation of melt permeability and related buoyancy-driven melt-solid  
333 segregation velocities (Figure s 3(c) and (d)). The relatively low inferred per-  
334 meabilities ( $\sim 10^{-14}\text{m}^2$ ) and melt-segregation velocities ( $\sim 20 \mu\text{m}/\text{yr}$ ) suggest  
335 that the  $\sim 0.4 \text{ vol}\%$  melt in and near the plume stem are practically immobile  
336 relative to the matrix, implying an important horizontal flow component of  
337 the matrix.

### 338 *3.2. The effect of Clapeyron slope, solid composition, and dihedral angle*

339 Figure 4(a) shows the histogram for the calculated thermal anomalies for  
340 three different values of the Clapeyron slope of olivine-wadsleyite transition.  
341 An increase in the Clapeyron slope from 2 MPa/K to 4 MPa/K, leads to a  
342 tighter probability distribution function centered around  $\Delta T = 0$ , with no  
343 visible shift of the median value of the distribution. The maps in panels (b)  
344 and (d) of Figure 4 show the calculated temperature anomaly distribution  
345 for two different values of the Clapeyron slope. The primary influence of  
346 the parameter Clapeyron slope is on the spread of the calculated thermal  
347 anomaly. In turn, the median of inferred melt volumes remains virtually  
348 unaffected by variations in Clapeyron slope (Figure 4(c)), since the central  
349 tendency of the probability distribution in panel (a) is insensitive to the  
350 variations in the Clapeyron slope.

351 In addition to the Clapeyron slope of the olivine-to-wadsleyite phase tran-  
352 sition, we also explore the effects of the solid-melt dihedral angle for different  
353 basalt fractions in the solid (Figure 5(a)). At higher dihedral angles, more  
354 melt is confined to grain corners, resulting in a smaller fraction of wetted grain



355 boundaries. This leads to more effective intergranular contacts and stronger  
356 skeletal networks of grains. To explain the calculated wave speed anomalies,  
357 therefore, a larger melt volume fraction is required (Hier-Majumder, 2008;  
358 Hier-Majumder and Abbott, 2010). But similar to the effects of recycled slab  
359 component, discussed next, this trade-off does not change our main conclu-  
360 sions.

361 Following the analysis of single crystals in Hawaiian lavas, Sobolev et al.  
362 (2007, 2005) estimated that the Hawaiian plume source contains approxi-  
363 mately 20% recycled slab component in addition to pyrolite. This basaltic  
364 component may be filtered near the top of the MTZ due to mechanical se-  
365 questration into a deep eclogitic pool (Ballmer et al., 2013; Cheng et al.,  
366 2015). Such a sequestration is promoted by a maximum of the negative den-  
367 sity anomaly of (silica-normative) basaltic materials in the depth range of  
368 about 300-410 km depth (Aoki and Takahashi, 2004). The mechanical se-  
369 questration of basalt-rich matrix into the deep eclogitic pool occurs by lateral  
370 spreading of this neutrally buoyant matrix just beneath the depth of den-  
371 sity inversion (Ballmer et al., 2013). The extent of the related segregation  
372 of basalt from the rest of the mantle, however, remains poorly constrained.  
373 While the lower limit of eclogite fraction  $f$  in the LVL is 20% (*i.e.* no segre-  
374 gation), the upper limit may be much higher. In this work, we report results  
375 for  $f = 27\%$ , *i.e.* near the lower bound.

376 Here, we quantify the effect of variable basalt fraction in the solid on  
377 the calculated melt-volume fractions (Figure 5, also see Figure 4(c)). We  
378 find that the reference wave speed increases with increasing  $f$ , well explained  
379 by the higher elastic moduli of eclogite compared to pyrolite. Accordingly,

380 more melt is required for higher  $f$  in order to explain the observed residual  
381 shear wave speed anomalies. In turn, smaller basalt contents yield smaller  
382 inferred melt fractions. Nevertheless, finite melt fractions in the LVL of a  
383 similar order of magnitude are always required for  $f \geq 20\%$ . Thus, our main  
384 conclusions remain robust independent of  $f$ . As shown in Figure 5, the same  
385 statement is true for the combined effects of  $f$  and solid-melt dihedral angle.

386 The maps in Figure 5(c) depict the distribution of melt vol% for four  
387 different volume fractions of  $f$ . As shown in the maps, with increasing  $f$ , the  
388 calculated melt volume fractions show an overall increase, but the pattern  
389 of melt distribution remains virtually unaffected. The most melt-rich region  
390 occurs to the east of the hot plume stem, near the 1580°C isotherm. Note  
391 that any finite melt fractions imply significant volatile fluxes to the LVL,  
392 due to the strongly incompatible behavior of H<sub>2</sub>O and CO<sub>2</sub> (Aubaud, 2004;  
393 Hirschmann and Dasgupta, 2009).

### 394 *3.3. The relationship between temperature and LVL thickness*

395 An important outcome of our analysis is that the thickness and internal  
396 structure of the LVL is clearly distinct from the temperature field inferred  
397 from MTZ thickness. As shown in Figure 6(a), there is no visible corre-  
398 lation between LVL thickness and temperature. In Figure 6(b), we plot  
399 the unprocessed amplitude of Ps conversion as a function of the calculated  
400 melt fractions. As the color of the symbols indicate, for a given measured  
401 amplitude, variations in melt fraction arise from variations in temperature,  
402 as their effects trade-off with each other. Once the effects of temperature  
403 are corrected for by subtracting the reference wave speed  $V_S^{ref}$ , the resid-  
404 ual anomaly only depends on melt fraction (Figure 6(d)). The color of the

405 points in Figure 6(c) show that higher melt fractions, up to 1.7 vol%, are  
406 associated with larger negative  $\Delta V_S$ . Ultimately, the residual  $\Delta V_S$  and the  
407 inferred melt fractions are not strongly controlled by temperature (*i.e.*, no  
408 correlation), consistent with our interpretation of volatile-assisted melting.

#### 409 3.4. Results from temperature calculations using 410 km topography

410 The maps in Figure 7 show the results of our inversion for melt content  
411 using the topography of the 410-km discontinuity to determine temperature,  
412 *i.e.* instead of MTZ topography. These calculations were carried out for a  
413 potential temperature of 1427°C, bulk excess eclogite fraction of 27%, a dihe-  
414 dral angle of 25°, and a Clapeyron slope of olivine to wadsleyite transition of  
415 3 MPa/K. The median melt volume fraction for this calculation is 0.3 vol%,  
416 similar to that obtained by using the MTZ thickness as a proxy for tempera-  
417 ture. As the maps indicate, the plume stem appears wider and the cold ‘halo’  
418 is substantially reduced in this approach compared to that shown in Figure  
419 2. As shown by the work of Tauzin and Ricard (2014), crustal effects above  
420 plumes can lead to overestimation of 410 km depth and introduce errors in  
421 the inferred temperature. Using the thickness of MTZ as a proxy eliminates  
422 this source of error. While we prefer the temperatures that are calculated  
423 from MTZ thickness, some earlier publications used 410-km topography as a  
424 proxy for temperature. Thus, we include this result for reference here.

## 425 4. Volatile fluxes from the leaky plume

426 The separation between thermal and chemical signatures provides us with  
427 an indication of the geodynamic processes operative within the Hawaiian

428 LVL. Based on our seismic observations and calculated melt volume frac-  
429 tions, two distinct patterns of flow within the LVL can be discerned when  
430 the map of temperature in Figure 2(c) is compared with the map of melt  
431 distribution in 3(b) (also the cartoon in 8(a)). First, dominantly vertical  
432 up and downwelling flows arising from mantle convection, driven by thermal  
433 buoyancy, are consistent with the inferred thermal structure in Figure 2(c).  
434 In turn, practically immobile melt fractions—evidenced by an average melt  
435 percolation speed of  $22 \mu\text{m}/\text{yr}$  within and near the plume conduit (Figure  
436 3(d))—indicate a second, dominantly horizontal flow of the plume matrix.  
437 Such spreading and stagnation of a “thermochemical” plume, which contains  
438 a significant fraction of basaltic material (with trapped melt) in addition to  
439 peridotite (Sobolev et al., 2007), can be caused by a sharp decrease of the  
440 buoyancy of basaltic material just above 410 km depth (Aoki and Takahashi,  
441 2004; Ballmer et al., 2013). Spreading and pooling of eclogitic material at the  
442 periphery of the Hawaiian plume at these depths is consistent with a regional  
443 joint-seismic tomography model(Cheng et al., 2015), as well as with a recent  
444 receiver-function study (Kemp et al., 2019), and provides a mechanism for the  
445 long-term stabilization and accumulation of melts away from the plume stem.  
446 As the incipient melt is dragged away from the hot plume stem, it does not  
447 freeze, because the pooling eclogitic material remains warm (Ballmer et al.,  
448 2013), and hence well above the volatile-rich solidi (Figure 8(b)). The leaked  
449 melt slowly accumulates outside the plume stem over time, explaining the  
450 observed higher melt content in comparison to the plume stem. The lateral  
451 extent of this melt accumulation can potentially include areas not covered by  
452 this study. We can use the seismic observation to further constrain the origin

453 of this melt. Comparison between the carbonated basalt (Thomson et al.,  
454 2016) and hydrous peridotite (Ohtani et al., 2004) solidi and our inferred  
455 temperatures (*i.e.*, 1440-1640°C; Figure 8(b)) illustrates that the observed  
456 melts must be generated by volatiles in the plume. It is important to no-  
457 tice that our melt fraction calculations were not constrained by any solidus,  
458 the coincidence of the seismically derived temperature and pressure and the  
459 solidi is thus completely independent of the rock physics analysis.

460 The leakage of melt from the Hawaiian plume leads to a substantial  
461 volatile flux back into the mantle. These lost volatiles may never reach the  
462 uppermost mantle, or even the atmosphere. Due to the strongly incompatible  
463 nature of H<sub>2</sub>O (Aubaud, 2004) and CO<sub>2</sub> (Hirschmann and Dasgupta, 2009),  
464 the observed 0.4 vol% partial melt can store 3.7 wt% H<sub>2</sub>O and 5.5 wt% CO<sub>2</sub>  
465 (see Appendix A), substantially higher than the measured concentrations of  
466 these volatiles in olivine-hosted melt inclusions from Hawaiian lavas (Hauri,  
467 2002). Using our observed LVL thicknesses and melt-volume fractions, as  
468 well as published partition coefficients and volatile abundances in the plume  
469 source, we estimate that the Hawaiian plume can leak between 0.7 and 10.7  
470 Mt/yr of CO<sub>2</sub> and between 0.6 and 1.9 Mt/yr of H<sub>2</sub>O to the LVL. For com-  
471 parison, the present day CO<sub>2</sub> surface flux at the Kilauea volcano is measured  
472 at 2.4 Mt/yr (Burton et al., 2013). Given the observed global correlations  
473 between plumes and LVLs (Vinnik and Farra, 2007), and this estimated loss  
474 to the LVL, the global CO<sub>2</sub> flux carried by plumes—before they enter the  
475 MTZ—needs to be significantly higher than the estimated 4–110 Mt/yr of  
476 CO<sub>2</sub> outgassed at hotspots (Dasgupta and Hirschmann, 2010). Similarly, sig-  
477 nificant amounts of H<sub>2</sub>O carried by mantle upwellings may never reach the

478 surface. These estimated fluxes demonstrate that LVLs act as gatekeepers  
479 for mantle volatiles, but are currently neglected in models of global volatile  
480 cycles (Dasgupta and Hirschmann, 2010; Kelemen and Manning, 2015; Plank  
481 and Manning, 2019). Additionally, the higher incompatibility of CO<sub>2</sub> rela-  
482 tive to H<sub>2</sub>O (Aubaud, 2004; Hirschmann and Dasgupta, 2009), coupled with  
483 the small degree of melting, will tend to preferentially sequester the former  
484 into the LVL and back into the deep mantle (Hirschmann and Dasgupta,  
485 2009). Such carbon enrichment of the LVL and deep mantle, a reservoir that  
486 has previously not been accounted for, can explain some or all of the miss-  
487 ing mantle carbon, reconciling the seemingly discrepant observation of lower  
488 C:H ratio in the known mantle reservoirs compared to chondritic meteorites  
489 (Hirschmann and Dasgupta, 2009). Further constraints on the global leak-  
490 age of volatiles at mantle plumes may advance our understanding of volatile  
491 delivery to Earth, and across the early solar system.

## 492 5. Conclusions

493 In this study, our rock physics analysis of teleseismic P-to-S conversions  
494 reveal the internal structure and melt distribution of the LVL above the  
495 Hawaiian MTZ. Our key conclusions are:

- 496 • The Hawaiian LVL is characterized by patches containing up to 1.7  
497 vol% melt outside the hot plume stem, while the regional melt distri-  
498 bution has a median of  $0.4 \pm 0.3$  vol%.
- 499 • The small melt volume fraction in the LVL, owing to reduced perme-  
500 ability, leads to a median melt segregation velocity of  $\sim 20$   $\mu\text{m}/\text{year}$ ,  
501 effectively trapping the melt within the matrix.

- 502 • The location of high melt concentration, coupled with low melt mobil-  
503 ity, suggests a possible lateral transport or leakage of matrix-trapped  
504 melt, away from the plume stem.
- 505 • Based on published petrological and geochemical data, we infer that  
506 the Hawaiian plume can leak up to 1.9 Mt/yr H<sub>2</sub>O and 10.7 Mt/yr CO<sub>2</sub>  
507 to the LVL.

### 508 **Acknowledgment**

509 C.A.R. and N.H. acknowledge funding from the Natural Environment  
510 Research Council (NE/M003507/1 and NE/K010654/1) and the European  
511 Research Council (GA 638665). SH-M acknowledges support from National  
512 Science Foundation, USA (EAR 1215800). The inversions on MuMaP were  
513 carried out on ARCHER.

### 514 **Appendix A. Calculation of volatile fluxes**

515 Based on our calculation of melt-migration velocities, which remain very  
516 small, we infer that the volatiles are carried away from the plume stem via im-  
517 mobile melt trapped in the triple grain junctions, i.e. by a laterally-spreading  
518 flow of the mantle matrix rather than melt percolation through the matrix.  
519 In this section, we present a zeroth order calculation of the flux of volatiles  
520 associated with the lateral spreading. Our calculations make a few simpli-  
521 fying assumptions, such as uniform leakage of melt around the plume stem  
522 and volatile concentration within the plume stem is equal to the source con-  
523 centration. While a detailed model of volatile leakage—capturing these com-  
524 plexities of the flow—is outside the scope of this article, the magnitude of

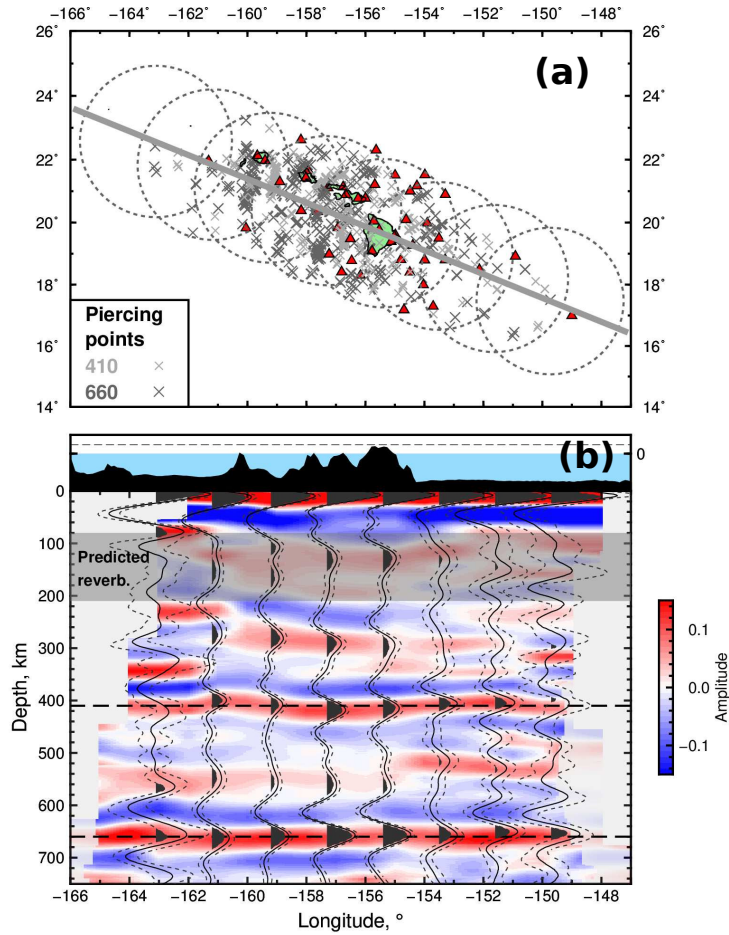


Figure 1: (a) The gray line across the map shows the location of the vertical cross section shown in the panel below. Red triangles are the seismic stations used for the bootstrap. Crosses are the corresponding piercing points at 410- and 660-km depth. (b) Vertical cross-sections through the 3-D depth migrated receiver functions calculated using a crust-corrected PREM wave speed model (Dziewonski and Anderson, 1981). Red and blue shades represent positive and negative amplitudes saturated at  $\pm 0.15$ , respectively. The image resolution is from a  $1^\circ$  by  $1^\circ$  latitude-longitude grid. Semi-transparent shades represent poorly constrained areas due to a low number of traces ( $< 5$ ). Black solid wiggles represent the stacked bin average for the respective area shown on the map above (dashed circles). Dashed wiggles are two standard deviations estimated from bootstrap analysis using 100 randomly selected subsets from within the respective bins. Gray shaded band indicates predicted crustal reverberations. 24



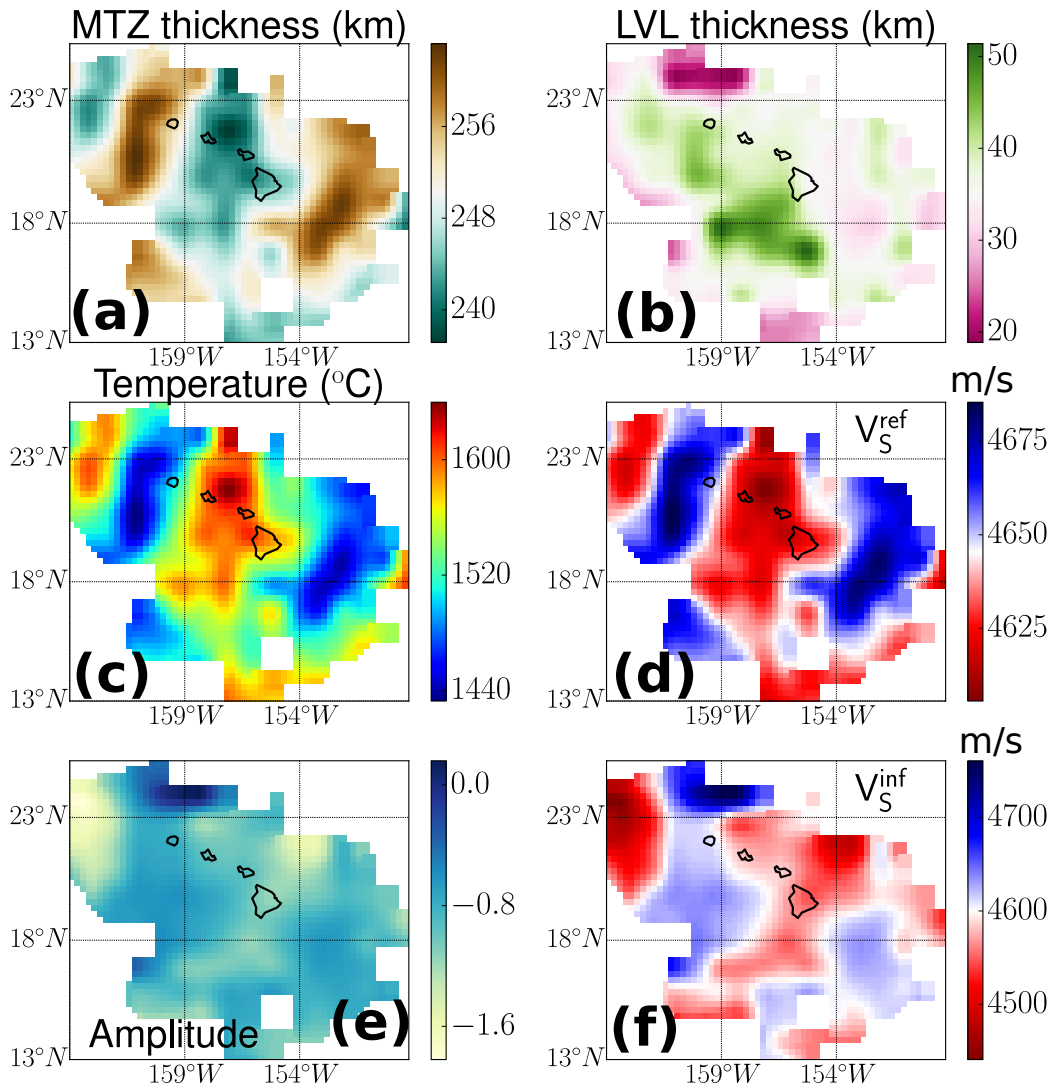


Figure 2: Map of the thermochemical anomalies above the transition zone. (a) Transition zone thickness measured from the Ps conversions. (b) Thickness of the LVL, measured by the distance between the LVL and the top of the MTZ using receiver functions (Agius et al., 2017). (c) The temperature at each point is calculated from the observed transition zone thickness for a mantle potential temperature of 1700 K and a Clapeyron slope for Olivine-Wadsleyite transition of 3 MPa/K. (d) Reference mantle wave speed calculated from the temperature at each point for a mantle eclogite fraction of 27%. (e) The observed amplitude of Ps conversion at the LVL normalized by the amplitude change atop the 410 km discontinuity. (f) The magnitude of shear wave speed calculated from the observed amplitude. (Hier-Majumder et al., 2014).

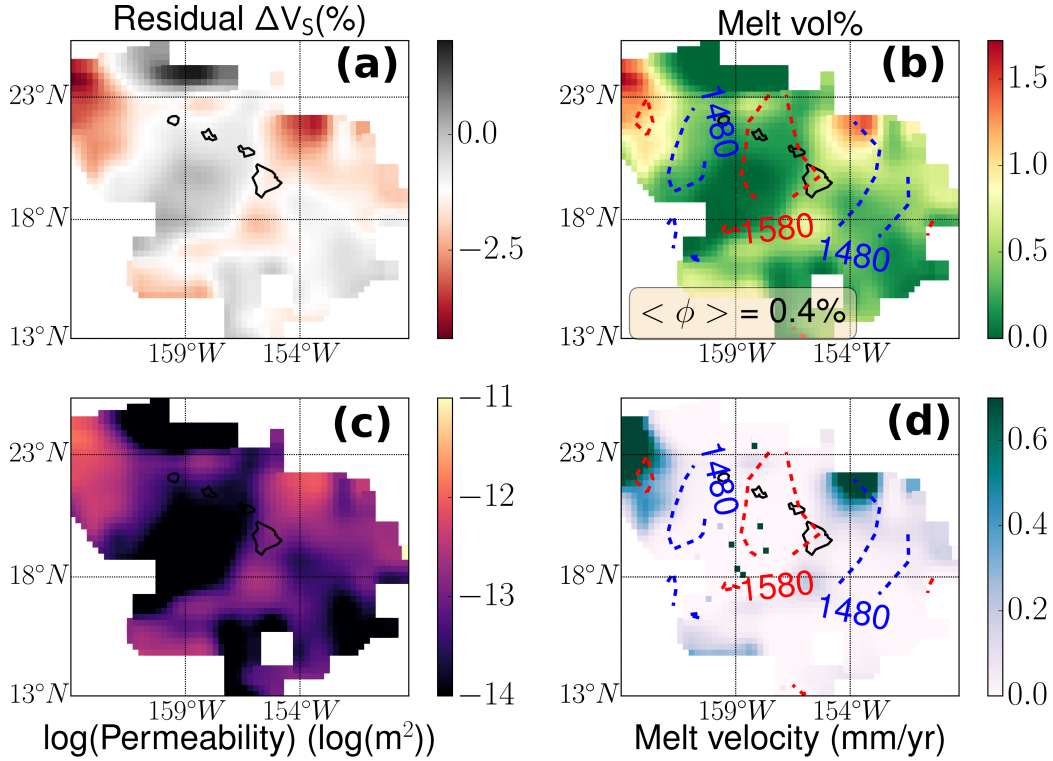


Figure 3: Melt distribution and flow, inferred from the normalized residual wave speed anomaly  $\Delta V_S$ . (a) Map of  $\Delta V_S$ , as calculated from  $V_S^{ref}$  and  $V_S^{inf}$ . (b) Map of melt volume fraction, as calculated from  $\Delta V_S$ , using a dihedral angle of  $25^\circ$  at the melt grain interface. (c) Map of melt permeability, as calculated from the melt volume fraction at each point using a model of melt tubules along triple grain junctions. The median value of the permeability is  $6.0 \times 10^{-14} \text{ m}^2$  (d) Buoyancy-driven segregation velocity of melt in a 1D compacting column, as calculated from an analytical solution of the compaction equations (Hier-Majumder and Courtier, 2011). The median value of the velocity is  $22 \text{ } \mu\text{m}/\text{yr}$ .

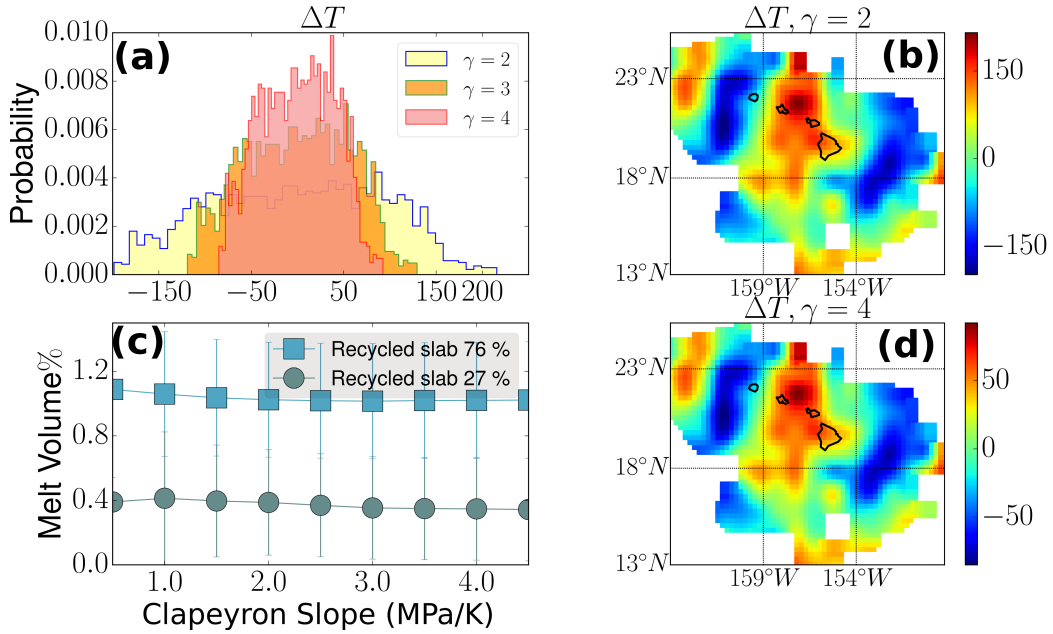


Figure 4: (a) Histogram showing the probability distribution of calculated temperature anomalies for three different values of Clapeyron slope ( $\gamma$ ) of the olivine-wadsleyite transition. Maps of the temperature anomalies for (b)  $\gamma = 2$  and (c)  $\gamma = 4$ . In Figure 4(c), the potential temperature has a constant value of 1700 K. (d) Plot of calculated median melt volume fraction as a function of the Clapeyron slope  $\gamma$ , used to calculate the temperature. Two series of data plots are shown for two different basalt fractions in the bulk composition.

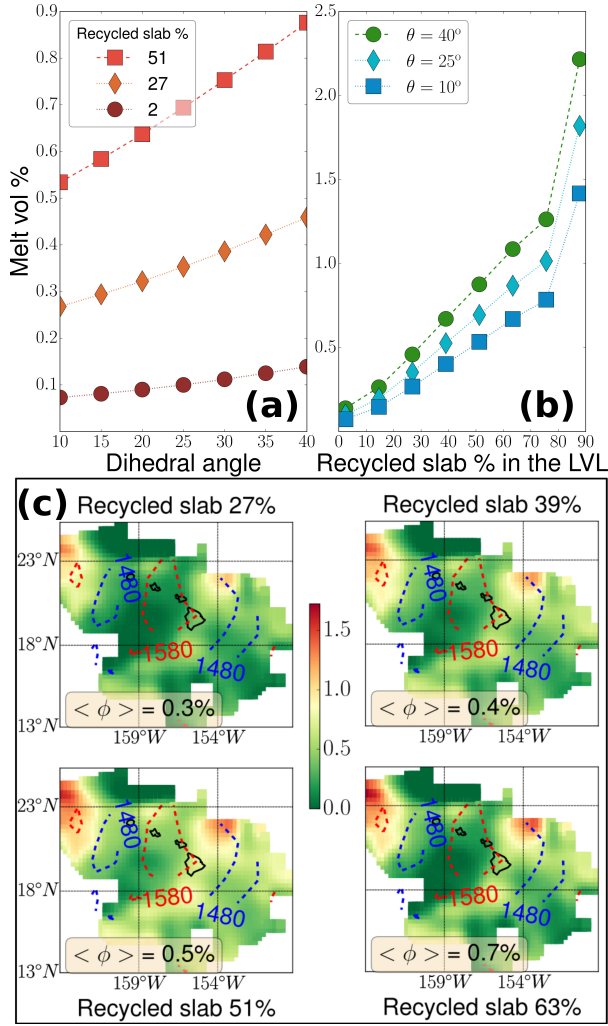


Figure 5: Plot of calculated median melt volume fraction as a function of (a) dihedral angle ( $\theta$ ) (b) and bulk composition (fraction of recycled slab in the mantle,  $f$ ). (c) Maps of melt volume % for four different values of  $f$ . Potential temperature is 1700 K and the dihedral angle is  $25^\circ$ . The value of median melt vol%,  $\langle \phi \rangle$  for each map is shown in the inset.

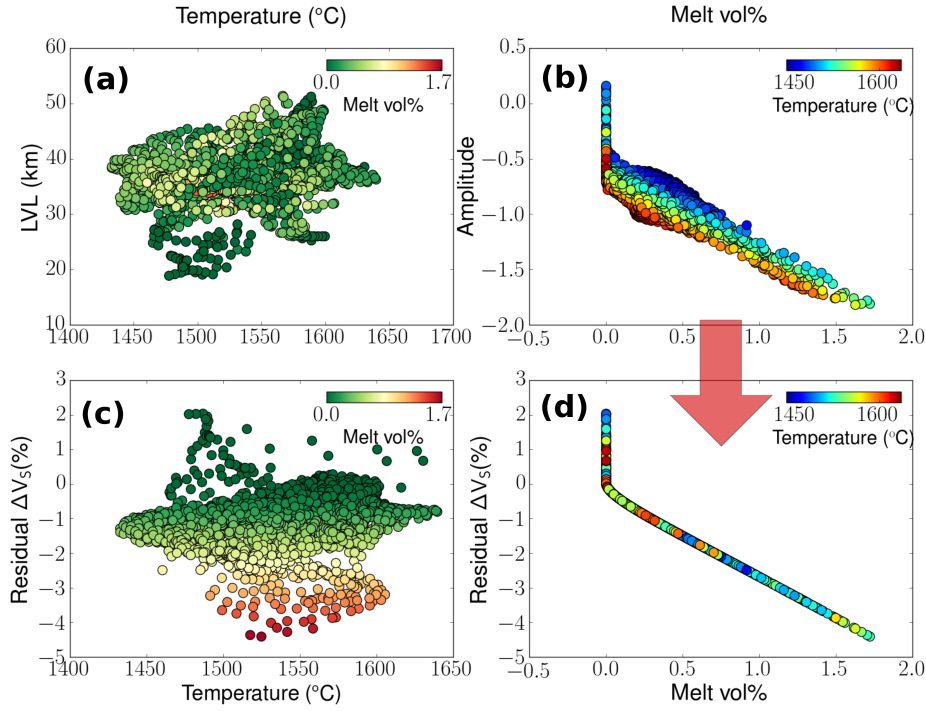


Figure 6: (a) Scatter plot of LVL thickness as a function of the calculated temperature for all data points in this study. The data points are colored by the melt volume fraction calculated at each location. (b) Plot of normalized P-S conversion amplitude as a function of calculated melt volume% at each location in the region. The data points are colored by the temperature at each location. (c) Scatter plot of temperature and the residual shear wave speed  $\Delta V_S$ . The data points are colored by the melt volume fraction. (d) The residual wave speed anomaly as a function of calculated melt volume%. The data points are colored by the temperature at each location. Spread in the observed amplitude is removed by the thermal correction indicated by the arrow between panels (b) and (d).

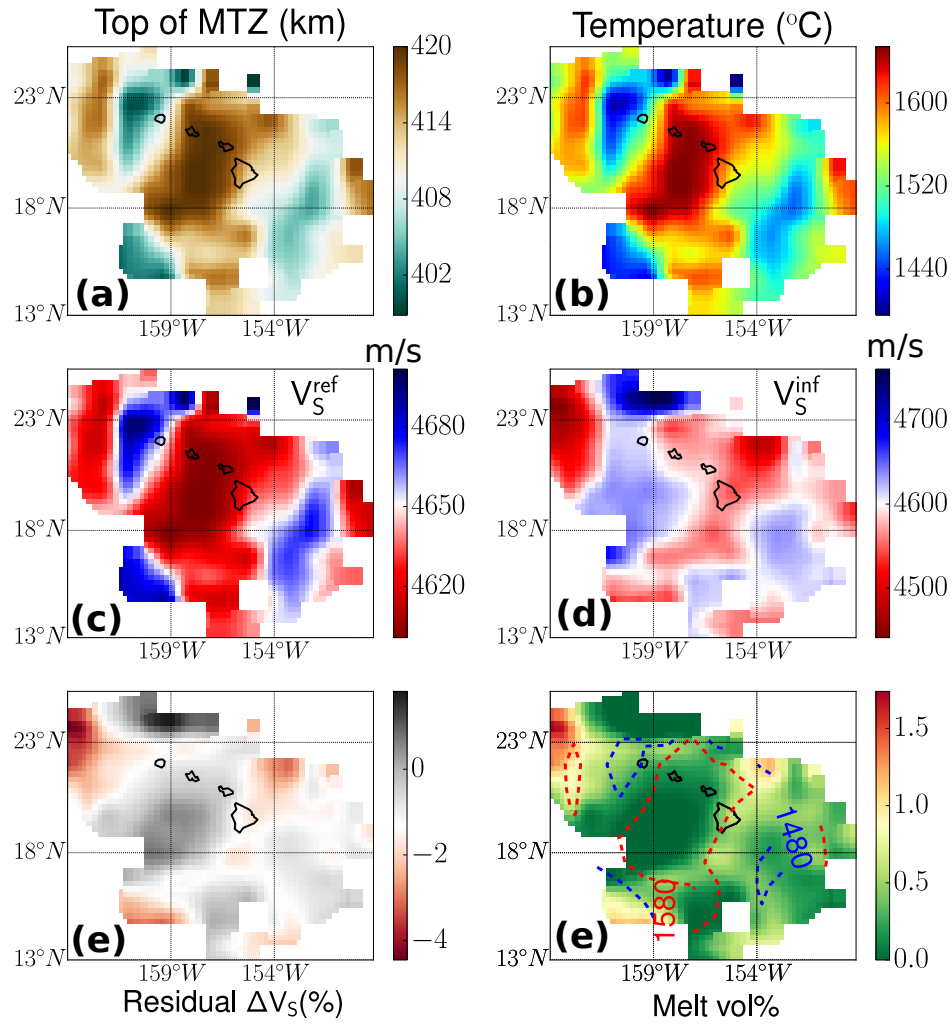


Figure 7: Map of analysis results using the 410 km topography (top of MTZ) to calculate the temperature. (a) Top of the MTZ shown in km. (b) Temperature calculated from the 410 km topography, (c) reference wave speed, (d) inferred wave speed, (e) residual  $\Delta V_S$  and (f) map of the calculated melt volume% with two isotherms overlain. For these maps, the other parameters are identical to that in Figures 1 and 2 of the main article.

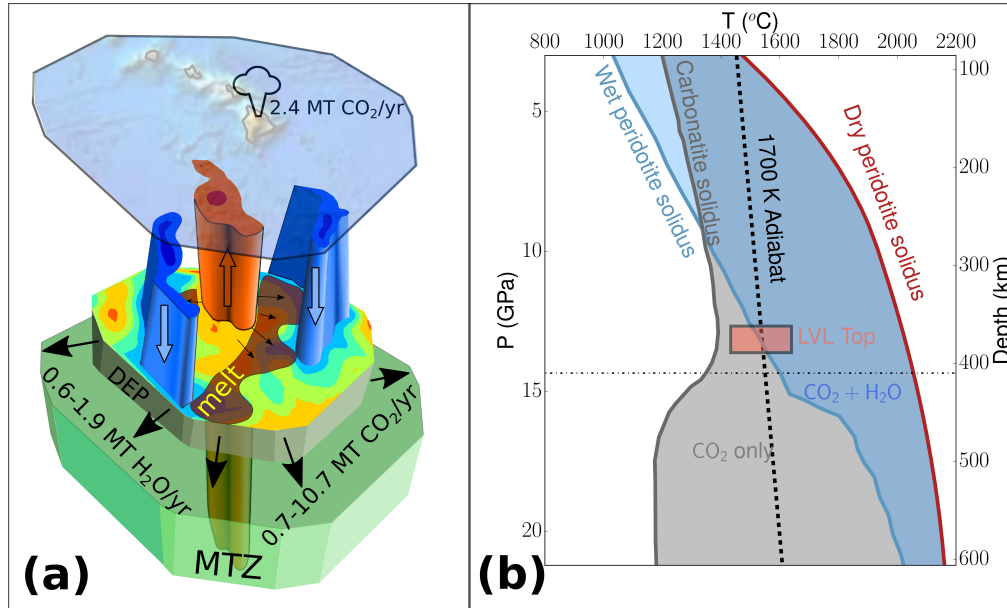


Figure 8: Mantle motion, volatile fluxes, and melting curves for the Hawaiian LVL. (a) A schematic diagram outlining melt leakage around the plume stem aided by lateral flow of a stagnated, spreading deep eclogite pool (DEP) atop the MTZ. The melt-rich regions are shaded in dark brownish red. (b) Solidi of carbonatite (Thomson et al., 2016) and hydrous peridotite (Ohtani et al., 2004) compared with the 1700 K adiabat. Width of the horizontal box corresponds to the range of temperature inferred from the transition zone thickness for the same adiabat. The vertical extent of the box depicts the range of LVL thicknesses inferred in this study.

525 volatile fluxes calculated by this simple approach highlights the importance  
 526 of this flux, currently ignored in global carbon cycle models.

527 With the caveat mentioned above, we derive the simple equation to cal-  
 528 culate the volatile flux. Assuming a horizontal mantle flow velocity of  $v$ , and  
 529 an LVL thickness of  $h$ , the total volume flow per unit time across the vertical  
 530 boundary of a cylindrical plume stem is given by  $2\pi rhv$ , where  $r$  is the radius  
 531 of the plume. If the melt volume fraction is given by  $\phi$ , and the melt density  
 532 by  $\rho_m$ , then the melt flow per unit time is  $2\pi rhv\phi\rho_m$ . Finally, for a volatile  
 533 concentration of  $c$  in the melt, the mass flow rate of the volatile is given by,  
 534  $2\pi rhv\phi\rho_m c$ .

535 While we do not have a direct way of measuring the concentration of  
 536 volatiles in the melt, we can use the estimates of the volatile concentration  
 537 near the center of the plume stem. If this source concentration is given as  $c_0$ ,  
 538 and the partition coefficient of the volatile is given by  $D^{solid/melt}$ , then using  
 539 the batch melting model, we get,

$$c = \frac{c_0}{(1 - D)\phi + D}. \quad (\text{A.1})$$

540 Using published values of  $D^{solid/melt}$ , we can calculate the concentration of  
 541 CO<sub>2</sub> and H<sub>2</sub>O in the LVL. For example, for  $D_C^{solid/melt} = 0.001$  (Hirschmann  
 542 and Dasgupta, 2009),  $D_H^{solid/melt} = 0.009$  (Aubaud, 2004), source concentra-  
 543 tions of CO<sub>2</sub> = 250 ppm (Anderson and Poland, 2017) and H<sub>2</sub>O = 450 ppm  
 544 (Bizimis and Peslier, 2015), and our median melt volume fraction of 0.0035,  
 545 we get 5.5 wt% CO<sub>2</sub> and 3.7 wt% H<sub>2</sub>O in the LVL. Next, we can use this  
 546 formula to calculate the fluxes of each of these volatiles away from the plume,

$$F = 2\pi rhv\phi\rho_m \left[ \frac{c_0}{(1 - D)\phi + D} \right]. \quad (\text{A.2})$$



547 We use the median values of LVL thickness,  $h = 35$  km, and melt volume  
548 fraction,  $\phi = 0.0035$ , from this study,  $\rho_m = 3400\text{kg/m}^3$  (Ghosh et al., 2007),  
549  $v = 10$  cm/yr (Ballmer et al., 2013), and  $r = 100$  km. To estimate the upper  
550 and lower bounds of  $\text{CO}_2$  and  $\text{H}_2\text{O}$  fluxes, we use the estimates of  $c_0 = 120$ -  
551  $1830$  ppm  $\text{CO}_2$  and  $c_0 = 300$ - $900$  ppm  $\text{H}_2\text{O}$  in the OIB source (Hirschmann  
552 and Dasgupta, 2009). These values lead to the flux ranges of  $0.7$  to  $10.7$   
553 Mt/yr of  $\text{CO}_2$  and  $0.6$  to  $1.9$  Mt/yr of  $\text{H}_2\text{O}$ , respectively.

554 **References**

- 555 Agius, M. R., Rychert, C. A., Harmon, N., Laske, G., 2017. Mapping the  
556 mantle transition zone beneath Hawaii from Ps receiver functions : Evi-  
557 dence for a hot plume and cold mantle downwellings. *Earth and Planetary*  
558 *Science Letters* 474, 226–236.
- 559 Anderson, K. R., Poland, M. P., 2017. Abundant carbon in the mantle be-  
560 neath Hawai'i. *Nature Geoscience* 10 (9), 704–708.
- 561 Aoki, I., Takahashi, E., 2004. Density of MORB eclogite in the upper mantle.  
562 *Physics of the Earth and Planetary Interiors* 143 (1-2), 129–143.
- 563 Aubaud, C., 2004. Hydrogen partition coefficients between nominally anhy-  
564 drous minerals and basaltic melts. *Geophysical Research Letters* 31 (20),  
565 2–5.
- 566 Ballmer, M. D., Ito, G., Wolfe, C. J., Solomon, S. C., 2013. Double layering  
567 of a thermochemical plume in the upper mantle beneath Hawaii. *Earth*  
568 *Planet. Sci. Lett.* 376, 155–164.
- 569 Bell, S. W., Forsyth, D. W., Ruan, Y., 2015. Removing noise from the vertical  
570 component records of ocean-bottom seismometers: Results from year one  
571 of the cascadia initiative. *Bulletin of the Seismological Society of America*  
572 105 (1), 300–313.
- 573 Bercovici, D., Karato, S., 2003. Whole-mantle convection and the transition  
574 zone water filter. *Nature* 425, 39–44.

- 575 Bercovici, D., Ricard, Y., Schubert, G., 2001. A two-phase model for com-  
576 paction and damage; 1, General theory. *Journal of Geophysical Research*,  
577 B, Solid Earth and Planets 106 (5), 8887–8906.
- 578 Bizimis, M., Peslier, A. H., 2015. Water in Hawaiian garnet pyroxenites:  
579 Implications for water heterogeneity in the mantle. *Chemical Geology* 397,  
580 61–75.
- 581 Burton, M. R., Sawyer, G. M., Granieri, D., 2013. Deep Carbon Emissions  
582 from Volcanoes. *Reviews in Mineralogy and Geochemistry* 75 (1), 323–354.
- 583 Cheng, C., Allen, R. M., Porritt, R. W., Ballmer, M. D., 2015. Seismic Con-  
584 straints on a Double-Layered Asymmetric Whole-Mantle Plume Beneath  
585 Hawai'i. In: Carey, R and Cayol, V and Poland, M and Weis, D (Ed.),  
586 HAWAIIAN VOLCANOES: FROM SOURCE TO SURFACE. Vol. 208 of  
587 Geophysical Monograph Book Series. Amer Geophys Union, pp. 19–34.
- 588 Crawford, W. C., Webb, S. C., 2000. Identifying and Removing TiltNoise  
589 from Low Frequency LT0.1Hz Seafloor Vertical Seismic Data. *Bulletin of*  
590 *the Seismological Society of America* 90 (4), 952–963.
- 591 Dasgupta, R., Hirschmann, M. M., 2010. The deep carbon cycle and melting  
592 in Earth's interior. *Earth Planet Sci. Lett* 298, 1–13.
- 593 Deuss, A. ., 2009. Global observations of mantle discontinuities using ss and  
594 pp precursors. *Surv. Geophys.* 30, 301–32.
- 595 Dziewonski, A. M., Anderson, D. L., 1981. Preliminary reference Earth  
596 model. *Physics of the Earth and Planetary Interiors* 25 (4), 297–356.

597 Ghosh, S., Ohtani, E., Litasov, K., Suzuki, A., Sakamaki, T., NOV 22 2007.  
598 Stability of carbonated magmas at the base of the Earth's upper mantle.  
599 GEOPHYSICAL RESEARCH LETTERS 34 (22).

600 Hauri, E., 2002. SIMS analysis of volatiles in silicate glasses, 2: Isotopes  
601 and abundances in Hawaiian melt inclusions. Chemical Geology 183 (1-4),  
602 115–141.

603 Hier-Majumder, S., DEC 11 2008. Influence of contiguity on seismic veloci-  
604 ties of partially molten aggregates. Journal of Geophysical Research-Solid  
605 Earth 113 (B12), B12205.

606 Hier-Majumder, S., Feb. 2020. sashgeophysics/mumap: Mumap v2.1.  
607 URL <https://doi.org/10.5281/zenodo.3673226>

608 Hier-Majumder, S., Abbott, M. E., OCT 15 2010. Influence of dihedral angle  
609 on the seismic velocities in partially molten rocks. Earth and Planetary  
610 Science Letters 299 (1-2), 23–32.

Hier-Majumder, S., Ballmer, M., Agius, M., Rychert, C., Harmon, N., 7  
2019. Hawaii LVL rock physics inversion data.  
URL [https://royalholloway.figshare.com/articles/dataset/Hawaii\\_LVL\\_rock\\_physics\\_inve](https://royalholloway.figshare.com/articles/dataset/Hawaii_LVL_rock_physics_inversion_data/10000000)

611 Hier-Majumder, S., Courtier, A., 2011. Seismic signature of small melt frac-  
612 tion atop the transition zone. Earth and Planetary Science Letters 308 (3-  
613 4), 334–342.

614 Hier-Majumder, S., Keel, E., Courtier, A., 2014. The influence of tempera-  
615 ture, bulk composition, and melting on the seismic signature of the low

616 velocity layer above the transition zone. *J. of Geophys. Res. Solid Earth*  
617 119.

618 Hier-Majumder, S., Ricard, Y., Bercovici, D., AUG 30 2006. Role of grain  
619 boundaries in magma migration and storage. *Earth and Planetary Science*  
620 *Letters* 248 (3-4), 735–749.

621 Hier-majumder, S., Tauzin, B., 2017. Pervasive upper mantle melting be-  
622 neath the western US. *Earth and Planetary Science Letters* 463, 25–35.

623 Hirschmann, M. M., Dasgupta, R., May 2009. The H/C ratios of Earth’s  
624 near-surface and deep reservoirs, and consequences for deep Earth volatile  
625 cycles. *Chemical Geology* 262 (1-2), 4–16.

626 Kelemen, P. B., Manning, C. E., 2015. Reevaluating carbon fluxes in subduc-  
627 tion zones, what goes down, mostly comes up. *Proceedings of the National*  
628 *Academy of Sciences* 112 (30), E3997–E4006.

629 Kemp, M., Jenkins, J., Maclennan, J., Cottaar, S., 2019. X-discontinuity and  
630 transition zone structure beneath hawaii suggests a heterogeneous plume.  
631 *Earth and Planetary Science Letters* 527, 115781.

632 Kohlstedt, D., Keppler, H., Rubie, D., 1996. Solubility of water in the  $\alpha$ ,  $\beta$   
633 and  $\gamma$  phases of  $(\text{Mg, Fe})_2\text{SiO}_4$ . *Contributions to Mineralogy and Petrology*  
634 123, 345–357.

635 Laske, G., Collins, J. A., Wolfe, C., Solomon, S., Detrick, R.S.and Orcutt,  
636 J. B. D., Hauri, E., 2009. Probing the hawaiian hot spot with new ocean  
637 bottom instruments. *EOS, Trans. Am. geophys. Un.* 90, 362–3.

- 638 Laske, G., Markee, A., Orcutt, J. A., Wolfe, C. J., Collins, J. A., Solomon,  
639 S. C., Detrick, R. S., Bercovici, D., Hauri, E. H., 2011. Asymmetric shal-  
640 low mantle structure beneath the Hawaiian Swell-evidence from Rayleigh  
641 waves recorded by the PLUME network. *Geophysical Journal International*  
642 187 (3), 1725–1742.
- 643 Laske, G., Masters, G. and Ma, Z., Pasyanos, M., 2013. Update on crust1.0 -  
644 a 1-degree global model of earths crust. p. 2658.
- 645 Leahy, G. M., Collins, J. A., Wolfe, C. J., Laske, G., Solomon, S. C., 2010.  
646 Underplating of the Hawaiian Swell: Evidence from teleseismic receiver  
647 functions. *Geophysical Journal International* 183 (1), 313–329.
- 648 Minarik, W., Watson, E. B., 1995. Interconnectivity of carbonate melt at low  
649 melt fraction. *Earth Planet Sci. Lett.* 133, 423–437.
- 650 Ohtani, E., Litasov, K., Tomofumi, H., Kubo, T., Kondo, T., jun 2004. Water  
651 transport into the deep mantle and formation of a hydrous transition zone.  
652 *Physics of The Earth and Planetary Interiors* 143-144, 255–269.
- 653 Plank, T., Manning, C. E., 2019. Subducting carbon. *Nature* 574 (7778),  
654 343–352.  
655 URL <http://dx.doi.org/10.1038/s41586-019-1643-z>
- 656 Rychert, C. A., Laske, G., Harmon, N., Shearer, P. M., 2013. Seismic imaging  
657 of melt in a displaced Hawaiian plume. *Nature Geoscience* 6 (8), 657–660.
- 658 Schulze, K., Marquardt, H., Kawazoe, T., Boffa Ballaran, T., McCammon,  
659 C., Koch-Müller, M., Kurnosov, A., Marquardt, K., 2018. Seismically in-  
660 visible water in Earth’s transition zone? *Earth and Planetary Science*

661 Letters 498, 9–16.  
662 URL <https://doi.org/10.1016/j.epsl.2018.06.021>

663 Shearer, P., 1990. Seismic imaging of upper-mantle structure with new evi-  
664 dence for a 520-km discontinuity. *Nature* 344, 121–126.

665 Sobolev, A. V., Hofmann, A. W., Kuzmin, D. V., Yaxley, G. M., Arndt,  
666 N. T., Chung, S.-L., Danyushevsky, L. V., Elliott, T., Frey, F. a., Garcia,  
667 M. O., Gurenko, A. a., Kamenetsky, V. S., Kerr, A. C., Krivolutsкая,  
668 N. a., Matvienkov, V. V., Nikogosian, I. K., Rocholl, A., Sigurdsson, I. a.,  
669 Sushchevskaya, N. M., Teklay, M., apr 2007. The amount of recycled crust  
670 in sources of mantle-derived melts. *Science (New York, N.Y.)* 316 (5823),  
671 412–7.

672 Sobolev, A. V., Hofmann, A. W., Sobolev, S. V., Nikogosian, I. K., 2005. An  
673 olivine-free mantle source of hawaiian shield basalts. *Nature* 434 (7033),  
674 590.

675 Sun, Y., Hier-Majumder, S., Xu, Y., Walter, M., 2020. Stability and migra-  
676 tion of slab-derived carbonate-rich melts above the transition zone. *Earth  
677 and Planetary Science Letters* 531, 116000.  
678 URL <https://doi.org/10.1016/j.epsl.2019.116000>

679 Tauzin, B., Debayle, E., Wittlinger, G., 2010. Seismic evidence for a global  
680 low-velocity layer within the Earth’s upper mantle. *Nature* 3, 718–721,  
681 doi:10.1038/NGEO969.

682 Tauzin, B., Ricard, Y., 2014. Seismically deduced thermodynamics phase di-

683 agrams for the mantle transition zone. *Earth and Planetary Science Letters*  
684 401, 337–346.

685 Thomson, A. R., Walter, M. J., Kohn, S. C., Brooker, R. A., 2016. Slab  
686 melting as a barrier to deep carbon subduction. *Nature* 1 (2005), 1689–  
687 1699.

688 Turcotte, D., Schubert, G., 2001. *Geodynamics*. John Wiley & Sons.

689 Vinnik, L., Farra, V., 2007. Low S velocity atop the 410-km discontinuity  
690 and mantle plumes. *Earth and Planetary Science Letters* 262, 398–412,  
691 doi:10.1016/j.epsl.2007.07.051.

692 Wei, S. S., Shearer, P. M., 2017. A sporadic low-velocity layer atop the 410km  
693 discontinuity beneath the Pacific Ocean. *Journal of Geophysical Research:*  
694 *Solid Earth* 122 (7), 5144–5159.

695 Wimert, J. T., Hier-Majumder, S., 2012. A three-dimensional microgeody-  
696 namic model of melt geometry in the earth’s deep interior. *Journal of*  
697 *Geophysical Research-Solid Earth* 117 (B04), B04203.

698 Wolfe, C. J., Solomon, S. C., Laske, G., Collins, J. a., Detrick, R. S., Orcutt,  
699 J. a., Bercovici, D., Hauri, E. H., Dec. 2009. Mantle shear-wave veloc-  
700 ity structure beneath the Hawaiian hot spot. *Science (New York, N.Y.)*  
701 326 (5958), 1388–90.

702 Wolfe, C. J., Solomon, S. C., Laske, G., Collins, J. a., Detrick, R. S., Orcutt,  
703 J. a., Bercovici, D., Hauri, E. H., Mar. 2011. Mantle P-wave velocity struc-  
704 ture beneath the Hawaiian hotspot. *Earth and Planetary Science Letters*  
705 303 (3-4), 267–280.



706 Xu, W., Lithgow-Bertolini, C., Stixrude, L., Ritsema, J., 2008. The effect  
707 of bulk composition and temperature on mantle seismic structure. *Earth*  
708 *Planet Sci. Lett.* 275, 70–79.

# Supplementary Material: Melt Leakage from the Hawaiian Plume above the Mantle Transition Zone

Saswata Hier-Majumder<sup>a</sup>, Maxim D. Ballmer<sup>b,c</sup>, Matthew Agius<sup>d</sup>,  
Catherine Rychert<sup>d</sup>, Nicholas Harmon<sup>d</sup>

<sup>a</sup>*Department of Earth Sciences, Royal Holloway University of London, Egham, Surrey,  
TW20 0EX, UK.*

<sup>b</sup>*ETH Zürich, Switzerland*

<sup>c</sup>*University College London, UK*

<sup>d</sup>*University of Southampton, UK*



---

*Email address: Saswata.Hier-Majumder@rhul.ac.uk (Saswata Hier-Majumder)*

*Preprint submitted to Physics of the Earth and Planetary Interiors      October 12, 2021*

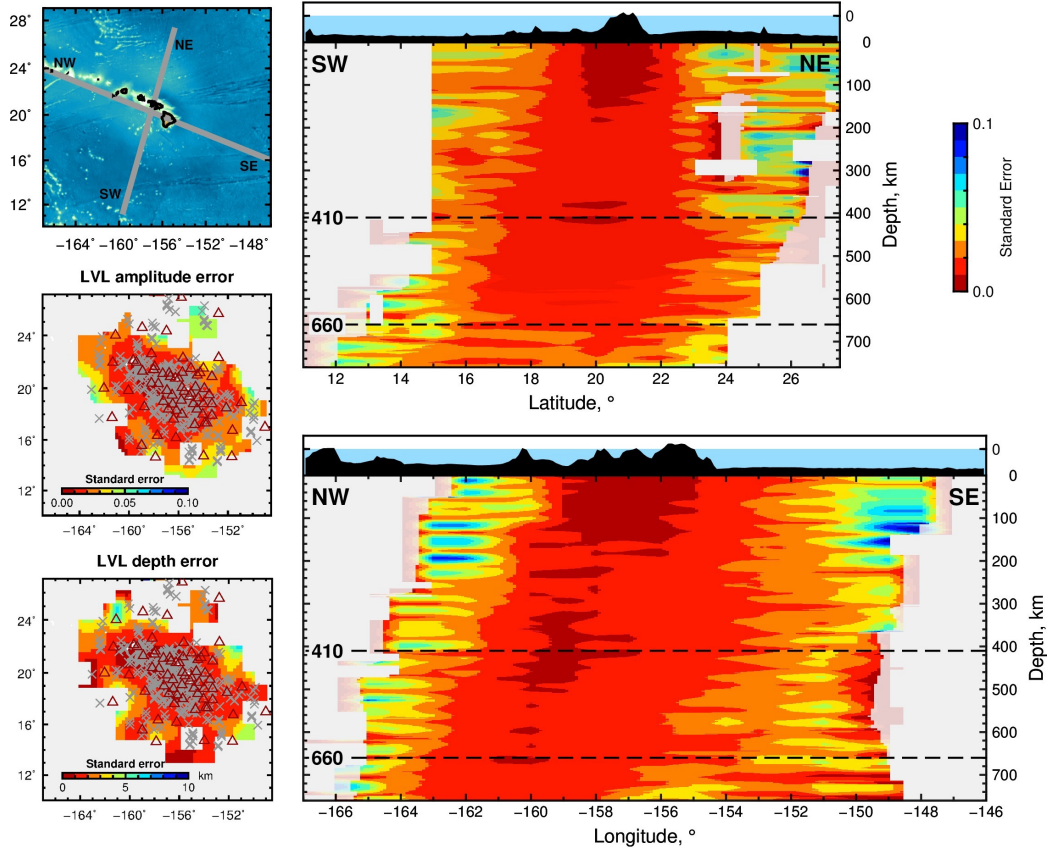


Figure 1: Vertical and horizontal cross sections showing errors for the amplitude across the entire depth range, and depth errors for the low-velocity layer (LVL). Red triangles are the seismic stations used. Crosses are piercing points at 410-km depth. Gray lines across top left map show the location of the vertical cross sections.